Exploring high frequency optoacoustic method for characterization of nanoparticles

Anuj Kaushik *, Ratan K. Saha

Department of Applied Sciences, Indian Institute of Information Technology Allahabad, Jhalwa, Allahabad 211015, India

ARTICLE INFO

ABSTRACT

Optoacoustic (OA) field computation by utilizing k-Wave simulation toolbox for six commonly used nanoparticles (NPs) has been performed. The characterization of NPs is often accomplished by the numerical simulation approach. Although, these simulation techniques are complicated, very costly, time-taking and arduous. Accordingly, there is a prerequisite for a fast, economical, and a simple simulation approach to comprehend the OA signal produced from different shapes of NPs. The technique has been employed to calculate the OA spectrum produced by nano size shapes [i.e. sphere, oblate, prolate, pentagon, hexagon, and star] over a large frequency band (10–200 GHz). The shapes of NPs were generated by utilizing simple mathematical equations. The first frequency minimum of OA spectrum approximately occurs at 48, 47, 80, 37, 58, and 57 GHz for nano sphere, oblate, prolate, pentagon, hexagon, and star, respectively when calculated in the direction of the symmetry axis. The same spectral feature appears nearly at 48, 22, 21, 32, 30, and 31 GHz, respectively, for those NPs when computed from the perpendicular direction. The NPs structure can be characterized by investigating single NP OA spectrum. The time taken by simulation for each NP is as short as the 12 min (simulated in the desktop having Intel(R) Core(TM) i7-6700U CPU working at 3.4 GHz and having 16 GB RAM) which is a remarkable increment over formerly communicated simulation time of a few hours employing analytical techniques.

1. Introduction

Optoacoustic (OA) imaging is a combined imaging technique that merges the attributes of the two, ultrasound and optical imaging modalities. The OA imaging has benefits of high level image contrast and high penetration depth (Wang and Hu, 2012; Wang, 2009; Xu and Wang, 2006). These advantages can be used for imaging the small animal brain, vasculature, breast cancer, and tumor angiogenesis (Li et al., 2015b; Peng et al., 2015; Ning et al., 2015; Wang et al., 2015; Nasiriavanaki et al., 2014; Matthews et al., 2014; Wang et al., 2013; Cai et al., 2011; Pramanik and Wang, 2009). When tissue is illuminated with a short laser pulse of suitable energy, the chromophores present in the tissue absorbs the light and cause local heating. As a consequence, thermoelastic expansion occurs followed by the generation of acoustic waves (OA signal). The ultrasound detectors are used to sense these OA waves (Xu and Wang, 2006). For deep tissue imaging, the near-infrared region is used. The optical absorption in this region is weak (Wang and Wu, 2012). So, we cannot have higher absorption at deeper depths. In order to enhance the amount of absorption, contrast agents are employed (Li and Chen, 2015; Nie L and Chen, 2014; Luke et al., 2013; Xi et al., 2012; Pan et al., 2012; Luke et al., 2012; Manohar et al., 2011;

Pan et al., 2011; Verawaty and Pramanik*, 2016; Kaushik et al., 2020b; Lu et al., 2010; Kim et al., 2010, 2009; Pan et al., 2009; Pramanik et al., 2009; X. Yang et al., 2007; Liu et al., 2007; Zhang et al., 2009).

Gold is a popular contrast agent in OA imaging (Li and Chen, 2015; Luke et al., 2013; Verawaty and Pramanik*, 2016; X. Yang et al., 2007; Zhang et al., 2009). In order to increase the optical absorption, the properties of gold nanoparticles (NPs) like shape, size, functionality are tuned (Hahn et al., 2011). The spherical shape of the gold NPs is used as an OA contrast agent for tumor diagnosis (Zhang et al., 2009). The gold NP with oblate and prolate shapes can be employed in medical imaging and microfluidics applications (Zhang et al., 2009). The NPs can also be coated with silica. This has a potential application for lymphatic imaging (Luke et al., 2013). The cylindrical carbon nanotubes, when present in the imaging system, were found to give stronger OA signal (Pramanik et al., 2009). A NP identical to red blood cell (RBC) shape has been found to circulate for a longer duration. It has also proved as an effective contrast agent (Zhang et al., 2009). Many researchers have also put efforts by designing experiments to synthesize different shapes and sizes of NPs following an OA analysis (Feis et al., 2014).

---

* Corresponding author.
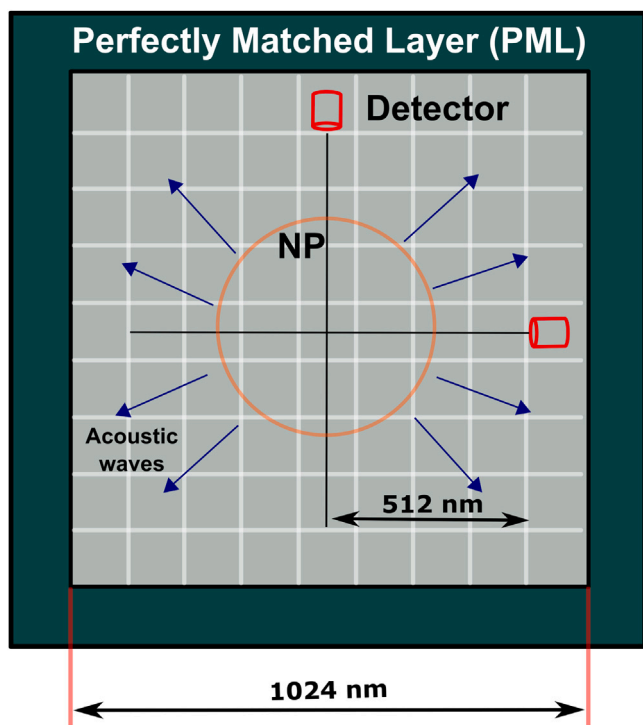*E-mail address:* rss2017503@iiita.ac.in (A. Kaushik).

Fig. 1. Demonstration of OA wave generation from a nanoparticle.

The experimental analysis of OA signals is difficult and time-consuming. Many mathematical studies have been developed recently to study the OA signal characteristics for cells and NPs (Feis et al., 2016; Kaushik et al., 2019b,a, 2020a; Li et al., 2015a; Saha et al., 2014; Saha, 2015). In one such computational study, the OA waves from RBCs and Michigan Cancer Foundation7 (MCF7 — a breast cancer cell line) nuclei were explained using spheroidal wave function (Li et al., 2015a). In another work, by employing the Green's function technique, the characteristics of OA signal were demonstrated for mixture of melanoma and RBCs (Saha, 2015). The OA response from cells with endocytosed gold NPs increased significantly without any alteration in thermophysical parameters and this simulation was carried out using Green's function approach (Saha et al., 2014). The finite element method was used to predict OA signals from Gold–Silver alloy NPs (Hatef et al., 2015). These computational methods aid in understanding the OA signal generation in a biological tissue without doing actual experiments. However, the computations can be complex and can take a longer time to execute. So, there is a requirement of a fast and simple method to simulate the OA signals. Our aim is to work to present such as fast and simple technique. We used six shapes of NPs to understand their OA signal characteristics. Only one type of NP was considered at a time. The OA spectrum is also given herein to demonstrate the variation of OA signal characteristics with different NP shapes.

The structure of this article as follows, Section 2 presents the materials and methods. The contour generation of each NP and physical parameters employed during OA field computation are briefly discussed in Section 3. Section 4 contains the results of this in silico study. The discussion and conclusions of this research paper are given in Section 5.

2. Materials and methods

2.1. OA signal calculation with k-wave

The mathematical background for the k-Wave toolbox is described in the literature (Treeby and Cox, 2010). Here, we briefly present it for culmination. The acoustic waves traveling through a compressible medium produce an effectual change in temperature, particle velocity, density and pressure, etc. These changes are included in the coupled first order partial differential equations. These coupled equations govern the conservation of mass, energy and momentum inside the medium. These three laws are combined to form a single second-order wave equation with acoustic pressure being the single variable in the equation. Classically, the first-order equations for a small-scale amplitude ultrasonic wave propagating through a nondispersive and homogeneous fluid media are written as Treeby and Cox (2010),

$$\frac{\partial u}{\partial t} = -\frac{1}{\rho_o} \nabla p, \tag{1}$$

$$\frac{\partial \rho}{\partial t} = -\rho_o \nabla . u, \tag{2}$$

$$p = c_o^2 \rho. \tag{3}$$

Here, u, p, ρ, ρ_0 and c_0 are the particle velocity, the acoustic pressure, the acoustic density, ambient density, and the isotropic sound-speed, respectively. The acoustic waves are generated when a portion of the fluid medium is heated due to the absorption of the laser pulse. In a immobile fluid medium with direction invariant acoustic properties, the sound generation is of thermoelastic nature. The viscosity and thermal conductivity of such a medium could be ignored. Under the said conditions, the acoustic wave equation can be obtained as,

$$\nabla^2 p - \frac{1}{c_o^2} \frac{\partial^2 p}{\partial t^2} = 0. \tag{4}$$

In k-Wave simulations, the coupled first-order equations are solved instead of equivalent second order wave equation. There are several reasons for doing this. The mass and force terms can be incorporated into these discrete equations easily. Also, pressure values and the particle velocity can be simulated on staggered grids for more accurate numerical solutions. It allows us to put an anisotropic absorbing layer around the computational domain to absorb the acoustic waves. This is called as a perfectly matched layer [PML]. Lastly, the acoustic intensity can also be computed using the particle velocity calculations.

An open source k-Wave toolbox (Treeby and Cox, 2010) was used for OA simulations in this study. The k-Wave when integrated to MATLAB allows a platform to create various geometric shapes, control detectors, and excitation laser parameters used in the OA simulations. The acoustic waves are seen propagating during the simulation process in the k-Wave. These waves coming from a geometric shape (mimicking a tissue or NP) appear as time domain OA signal. The schematic of an OA setup is shown in Fig. 1. It consists of a 2D computational grid having 1024×1024 pixels with a surrounding perfectly matched layer (PML) to prevent boundary reflections. The size of each voxel is taken as 1 nm. A homogeneous medium has been considered for this study i.e. the medium having no acoustic absorption/attenuation or dispersion of sound.

A single NP, placed at the center of the computational domain, was used as a target object. The number of time steps was 1000 with a time step of duration of 92 femtoseconds. The incident light pulse exciting the NP was considered to be homogeneous and hence a homogeneous initial pressure distribution within the NP is assumed. An ideal delta pulse is assumed for excitation. We placed the ideal point detector at a distance of 512 nm from the center of the computational domain. In order to check the variation in OA spectrum with the location of the sensor, we placed the detector at two different locations, one along the axis of symmetry and the other perpendicular to this axis of symmetry. We employed six geometric shapes of NPs. These were sphere, prolate, oblate, pentagon, hexagon, and star as illustrated in Fig. 2. These shapes exhibit suitable characteristics as contrast agents in OA imaging. The diameter of sphere shaped NP was 120 nm. Due to the restriction of pixel size, wide range dimensions were unavoidable.
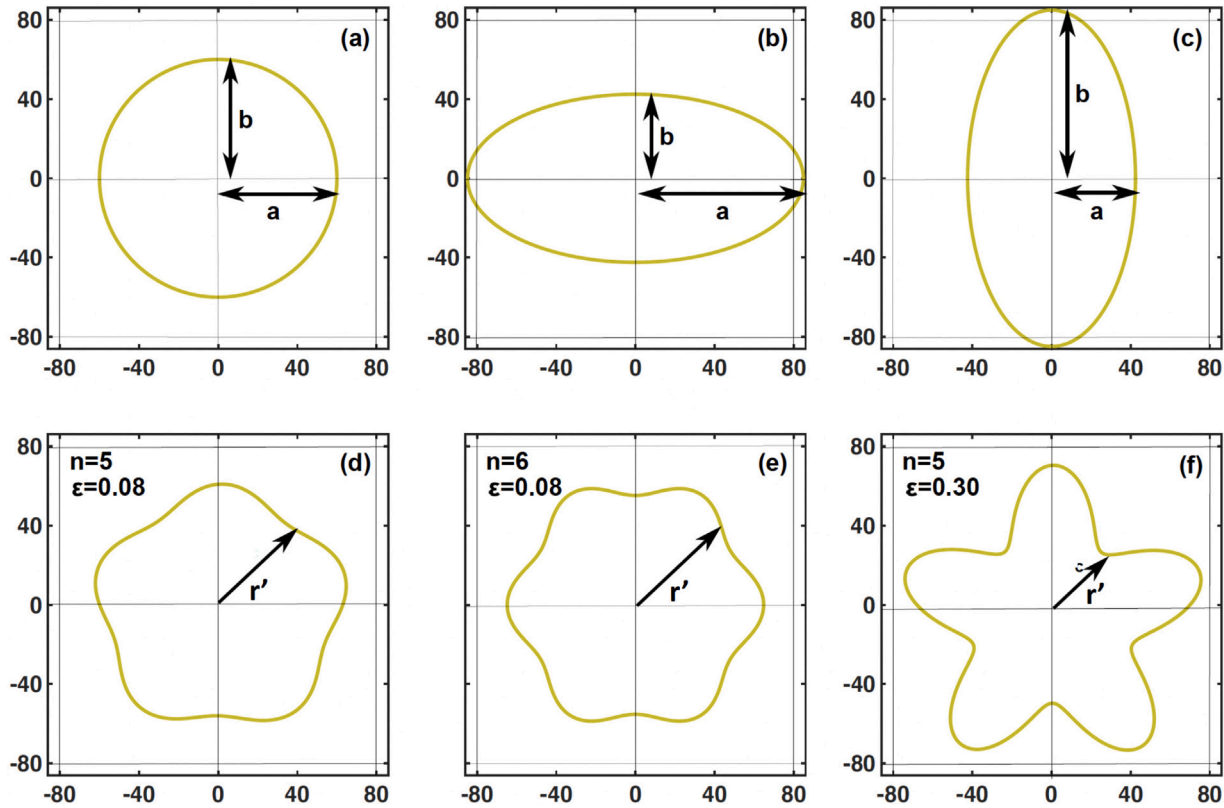
Fig. 2. (a–f) Representative plots of nano sphere, oblate, prolate, pentagon, hexagon and star shapes.

3. Numerical simulation parameters

3.1. Physical parameters

A 3240 m/s was taken as the speed of sound of the medium (this is the speed of sound in gold metal) and $\rho = 19300$ kg/m^3 was chosen as the density of the medium (Li and Chen, 2015). For simplicity, no dispersion of sound or absorption condition has been employed to make an acoustically homogeneous medium. The k-Wave itself fixed the other optical and thermo-mechanical properties. The OA source was too positioned at the center of simulation grid. All calculations were done on a personal computer with specifications (Intel(R) Core(TM) i7-6700U CPU working at 3.4 GHz and having 16 GB RAM). To calculate the OA field amplitude for each NP shape, approximately 12 min were taken by the computer.

3.2. Shape parameters

3.2.1. Nano sphere, oblate and prolate shapes

A spheroid can be generated by rotating an ellipse either about its major axis or its minor axis. Accordingly, they are known as nano prolate and oblate spheres, respectively. The radial distance of a point on the surface of such an object is given by (see Fig. 2(a–c)),

$$r'(\theta') = \frac{ab}{[b^2 \sin^2 \theta' + a^2 \cos^2 \theta']^{1/2}}, \tag{5}$$

with a and b are the semi-axes. For prolate sphere $b > a$ and for oblate sphere $b < a$. Three representative shapes of spheroidal NPs are shown in Fig. 2(a–c). In this work, we have studied how OA spectrum changes for different spheroidal NPs. All the shape-related parameters are given in Table 1.

Table 1
Numerical values for shape parameters used in calculation. (The unit for length parameters is in nm.)

Objects	Surface area (nm^2)	Shape parameters
Nano sphere	1.13×10^4	$a = 60.0$, $b = 60.0$
Nano oblate	1.13×10^4	$a = 84.84$, $b = 42.42$
Nano prolate	1.13×10^4	$a = 42.42$, $b = 84.84$
Nano pentagon	1.13×10^4	$R_c = 60$, $\epsilon = 0.08$, $n = 5$
Nano hexagon	1.13×10^4	$R_c = 60$, $\epsilon = 0.08$, $n = 6$
Nano star	1.13×10^4	$R_c = 60$, $\epsilon = 0.30$, n = 5

3.2.2. Nano pentagon, hexagon and star particles

The nano pentagon, hexagon and star shapes were produced utilizing the following equation,

$$r'(\theta') = R_c[1 + \epsilon T_n(\cos \theta')], \tag{6}$$

where $T_n(\cos \theta') = \cos n\theta'$ is the Chebyshev polynomial of degree n, n indicates to the waviness parameter, R_c is the radius of the unperturbed sphere and ϵ is the deformation parameter (Mugnai and Wiscombe, 1986). The pentagon, hexagon, and star shapes were obtained for n = 5, 6, 5 and ϵ = 0.08, 0.08, and 30, respectively.

4. Results

The spectral behavior of the nano sphere is presented in Fig. 3(a) along and perpendicular to the symmetry axis, respectively. It is observed that OA spectral features are the same for both the detector locations. It is because of the symmetrical shape of nano sphere. In this case, the first minimum appears at 48 GHz for both the positions of ultrasonic detector. From 1 to 10 GHz, the OA spectrum is flat and featureless for a nano sphere as illustrated in Fig. 3(a).
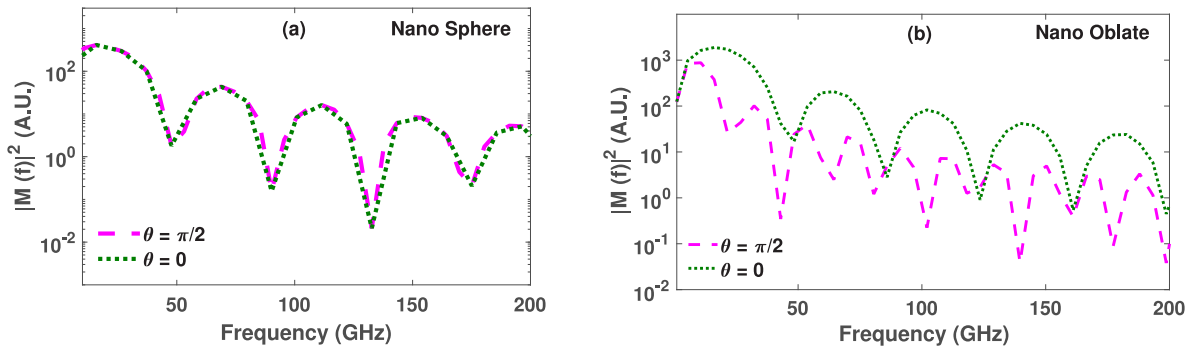
Fig. 3. (a) Graphs of the OA spectral power computed at 0 and $\pi/2$ as a function of frequency (10–200 GHz) for nano sphere. (b) Same as (a) but for nano oblate.
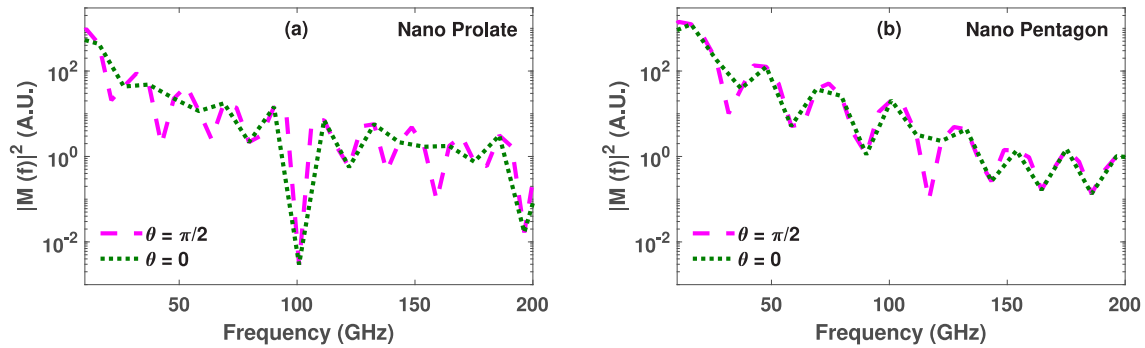

Fig. 4. (a) Plots of the OA field magnitude calculated at 0 and $\pi/2$ as a function of frequency (10–200 GHz) for nano prolate. (b) Same as (a) but for nano pentagon.
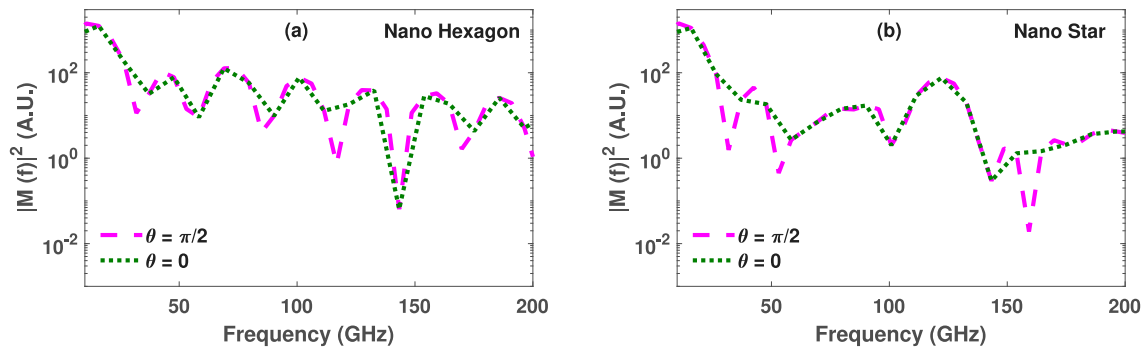

Fig. 5. (a) Graphs of the OA spectral power calculated at 0 and $\pi/2$ as a function of frequency (10–200 GHz) for nano hexagon. (b) Same as (a) but for nano star.

The graphs of $|M(f)|^2$ for a nano oblate and prolate is presented in Figs. 3(b) and 4(a) for two sensor positions ($\theta = 0$ and $\theta = \pi/2$) relative to the Z-axis, see Fig. 1. The first spectral dip for oblate exhibits at 47 and 22 GHz, respectively. This object is really thin along this direction (see Fig. 2(b)) and that pushes the first dip to appear at a high frequency. Though, the first dip for the second plot occurs at around 80 GHz. The thickness of the prolate in this direction is 41.4% greater than the nano sphere, respectively. That is why the dip pops up before as compared to nano sphere. The spectra corresponding to the pentagon, and hexagon are demonstrated in Figs. 4(b) and 5(a), respectively. The first minimum position for these NPs occurs at 37 and 58 GHz, respectively.

The width of star NP along the direction of symmetry is little more than that of nano sphere. That is why the first dip of the star is observed at 57 GHz in the direction of $\theta = 0$. The first minimum becomes noticeable at 31 GHz, when computed perpendicular to the direction of symmetry, the location of this minimum is explained by the broadness along the side view.

Along with the location of first dip, the number of minimum positions also differentiate the various shapes. The number of dips are

different for each NP along each measurement direction. The number of minimum corresponding to the sphere, oblate, prolate, pentagon, hexagon, and star is 4, 5, 4, 7, 6, and 5, respectively.

5. Discussion and conclusions

Different spectrum representing lines for nano sphere, oblate, prolate, pentagon, hexagon, and star have been produced at two sensor locations ($\theta = 0$ and $\pi/2$). For this purpose k-Wave simulation toolbox is employed. Here we computed all simulations in two-dimensional (2D) environment. It is observed that spectral lines are unique for all NPs taken in this paper. However, acoustic properties for the source and surrounding medium are considered same in the k-Wave simulations. The wave number of a wave depends upon the speed of sound in the NPs and hence moves the locations of minimum. Here we constricted this study up to six different shapes. However, there are many shapes like cube, triangle etc. We can too perform this simulation in three dimensional (3D) computational grid, but that will be tedious as compared to 2D computational grid.

The spectrum trademark reflected in the frequency spectrum could be truly valuable in recognizing the shape of a NP too. Additionally, these sorts of simulation demanded less intricate coding and computationally less requesting. With the expressed PC specifications utilized, it took around 12 min to finish one set of simulations for one structure of NP. This simulation time is much faster than recently revealed analytical techniques, which needs a couple of hours to produce the OA signals (Hatef et al., 2015). An ideal point ultrasonic sensor was used to capture the acoustic waves. This investigation can also be done with more realistic and complex ultrasonic detectors depending upon the need. At present just the impact of shape and size are examined here, the properties of the NPs, for example, absorption coefficient can likewise be modified for more detailed investigation. An ideal laser pulse excitation is employed for each simulation. Although, in practical applications the pulse width of laser excitation is in the range (2–12 ns). These adjustments can easily be included in the solution of the Helmholtz wave equation (in k-Wave). Different pulse width can be applied based on the satisfaction of thermal confinement conditions. However, here the width of pulse is very small and hence satisfy the thermal confinement condition even for a nanoscale target size. We also assumed that the ultrasound detector has infinite detection bandwidths. However in practical approach, ultrasound detectors of finite bandwidth are utilized to capture the OA signals. For OA imaging of single cells, ultra-high frequency transducers were employed. In such a work, transducers with a center frequency of 1.2 GHz was used (Strohm et al., 2013). In our study, we have considered ideal point detectors with infinite bandwidth.

The joint impact of infinite ultrasound detection bandwidth and an ideal excitation laser pulse width generates a very wide frequency spectrum of the captured OA signals. However, with finite ultrasound detector bandwidth and finite excitation laser pulse width, we cannot obtain such a high frequency OA spectrum. Overall, we have observed that there is a identifiable spectral signature of the shape of the NP to the optoacoustic signal produced and its frequency spectrum. Albeit, quantitatively differentiation has not been made for all shapes. As the point of the investigation was to exhibit that, it is conceivable to utilize an user-friendly toolbox to generate optoacoustic signal from NPs.

In conclusion, the k-Wave simulation toolbox is utilized to capture the OA signal and accordingly the OA spectrum has been produced by a single NP (having various shapes). Six different structures of NPs is simulated namely sphere, oblate, prolate, pentagon, hexagon, and star. The frequency spectrum was computed using simulation means. It was seen that there is a distinguishable alteration in the OA spectrum depending on the shape of each NP. These distinctions can be valuable to identify the shape of NP. This simulation technique is inexpensive, simple, and does not need any prior complex mathematical modeling. Further, the properties (i.e. the surrounding medium and absorption coefficient) of NPs may be varied if required. This simulation technique allows a better understanding on which shapes of NPs might act as contrast agents for OA imaging.

CRediT authorship contribution statement

Anuj Kaushik: Conceptualization, Methodology, Software, Validation, Data curation, Writing – original draft. **Ratan K. Saha:** Visualization, Investigation, Writing – review & editing, Supervision.

Declaration of competing interest

The authors declare that they have no known competing financial interests or personal relationships that could have appeared to influence the work reported in this paper.

Acknowledgment

References

Cai, X., Kim, C., Pramanik, M., Wang, L.V., 2011. Photoacoustic tomography of foreign bodies in soft biological tissue. J. Biomed. Opt. 16 (4), 046017.

Feis, A., Gellini, C., Salvi, P.R., Becucci, M., 2014. Photoacoustic excitation profiles of gold nanoparticles. Photoacoustics 2 (1), 47–53.

Feis, A., Gellini, C., Salvi, P.R., Becucci, M., 2016. Simulating photoacoustic waves from individual nanoparticle of various shapes using k-wave. Biomed. Phys. Eng. Express 2 (1), 035013.

Hahn, M., Singh, A., Sharma, P., Brown, S., Moudgil, B., 2011. Nanoparticles as contrast agents for in-vivo bioimaging: current status and future perspectives. Anal. Bioanal. Chem. 399 (1), 3–27.

Hatef, A., et al., 2015. Analysis of photoacoustic response from gold–silver alloy nanoparticles irradiated by short pulsed laser in water. J. Phys. Chem. C 119 (42), 24075–24080.

Kaushik, A., Sonker, D., Saha, R.K., 2019a. Use of Angular Distribution of Differential Photoacoustic Cross-Section Data for Estimating Source Size. SPIE, 10770E.

Kaushik, A., Sonker, D., Saha, R.K., 2019b. Study on angular distribution of differential photoacoustic cross-section and its implication in source size determination. J. Opt. Soc. Amer. A 36, 387–396.

Kaushik, A., Yallavarthy, P.K., Saha, R.K., 2020a. Convergent Born series improves accuracy of numerical solution of time independent photoacoustic wave equation. J. Modern Opt. 67 (9), 849–855.

Kaushik, et al., 2020b. A Simulation Study for Characterization of the Nanoparticles By Exploiting Optoacoustic Effect. Laser Science Optical Society of America, JTu1B-18.

Kim, C., Favazza, C., Wang, L.V., 2010. In vivo photoacoustic tomography of chemicals: high-resolution functional and molecular optical imaging at new depths. Chem. Rev. 110 (5), 2756–2782.

Kim, J.W., Galanzha, E.I., Shashkov, E.V., Moon, H.M., Zharov, V.P., 2009. Golden carbon nanotubes as multimodal photoacoustic and photothermal high-contrast molecular agents. Nat. Nanotechnol. 4 (10), 688–694.

Li, W., Chen, X., 2015. Gold nanoparticles for photoacoustic imaging. Nanomedicine 10 (2), 299–320.

Li, Y., Fang, H., Min, C., Yuan, X., 2015a. Simulating photoacoustic waves produced by individual biological particles with spheroidal wave functions. Sci. Rep. 5, 14801.

Li, X., Heldermon, C.D., Yao, L., Xi, L., Jiang, H., 2015b. High resolution functional photoacoustic tomography of breast cancer. Med. Phys. 42 (9), 5321–5328.

Liu, Y., et al., 2007. The shape of things to come: importance of design in nanotechnology for drug delivery. Ther. Deliv. 3 (2), 064701.

Lu, W., et al., 2010. Photoacoustic imaging of living mouse brain vasculature using hollow gold nanospheres. Biomaterials 31 (9), 2617–2626.

Luke, G.P., Bashyam, A., Homan, K.A., Makhija, S., Chen, Y.S., Emelianov, S.Y., 2013. Silica-coated gold nanoplates as stable photoacoustic contrast agents for sentinel lymph node imaging. Nanotechnology 24 (45), 455101.

Luke, G.P., Yeager, D., Emelianov, S.Y., 2012. Biomedical applications of photoacoustic imaging with exogenous contrast agents. Ann. Biomed. Eng. 40 (2), 422–437.

Manohar, S., Ungureanu, C., Van Leeuwen, T.G., 2011. Gold nanorods asmolecular contrast agents in photoacoustic imaging: the promises and the caveats. ContrastMediaMol. I 6 (5), 389–400.

Matthews, T.P., Zhang, C., Yao, D.K., Maslov, K., Wang, L.V., 2014. Label-free photoacoustic microscopy of peripheral nerves. J. Biomed. Opt. 19 (1), 016004.

Mugnai, A., Wiscombe, W.J., 1986. Scattering from nonspherical Chebyshev particles. I: cross sections, single-scattering albedo, asymmetry factor and backscattered fraction. Appl. Opt. 25 (7), 1235–1244.

Nasiriavanaki, M., Xia, J., Wan, H., Bauer, A.Q., Culver, J.P., Wang, L.V., 2014. High-resolution photoacoustic tomography of resting-state functional connectivity in the mouse brain. Proc. Natl. Acad. Sci. 111 (1), 21–26.

Nie L., Chen, X., 2014. Structural and functional photoacoustic molecular tomography aided by emerging contrast agents. Chem. Soc. Rev. 43 (20), 7132–7170.

Ning, B., et al., 2015. Simultaneous photoacoustic microscopy of microvascular anatomy, oxygen saturation, and blood flow. Opt. Lett. 40 (6), 910–913.

Pan, D., et al., 2009. Molecular photoacoustic tomography with colloidal nanobeacons. Angew. Chem. 121 (23), 4170–4173.

Pan, D., et al., 2011. Molecular photoacoustic imaging of angiogenesis with integrin-targeted gold nanobeacons. FASEB J. 25 (3), 875–882.

Pan, D., et al., 2012. Photoacoustic sentinel lymph node imaging with self-assembled copper neodecanoate nanoparticles. Acs Nano 6 (2), 1260–1267.

Peng, K., He, L., Wang, B., Xiao, J., 2015. Detection of cervical cancer based on photoacoustic imaging—the in-vitro results. Biomed. Opt. Express 6 (1), 135–143.

Pramanik, M., Swierczewska, M., Green, D., Sitharaman, B., Wang, L.V., 2009. Single-walled carbon nanotubes as a multimodal-thermoacoustic and photoacoustic-contrast agent. J. Biomed. Opt. 14 (3), 034018.

Pramanik, M., Wang, L.V., 2009. Thermoacoustic and photoacoustic sensing of temperature. J. Biomed. Opt. 14 (5), 054024.

Saha, R.K., 2015. A simulation study on the quantitative assessment of tissue microstructure with photoacoustics. IEEE Trans. Ultrason. Ferroelectr. Freq. Control 62 (5), 881–895.

Saha, R.K., Roy, M., Datta, A., 2014. Simulation study on the photoacoustics of cells with endocytosed gold nanoparticles. Curr. Sci. 106, 1554–1559.

Strohm, E.M., Berndl, E.S., Kolios, M.C., 2013. High frequency label-free photoacoustic microscopy of single cells. Photoacoustics 1, 49–53.

Treeby, B.E., Cox, B.T., 2010. K-wave: MATLAB toolbox for the simulation and reconstruction of photoacoustic wave fields. J. Biomed. Opt. 15 (2), 021314.

Verawaty, Pramanik*, M., 2016. Simulating photoacoustic waves from individual nanoparticle of various shapes using k-waves. Biomed. Phys. Eng. Express 2 (3), 035013.

Wang, L.V., 2009. Multiscale photoacoustic microscopy and computed tomography. Nat. Photonics 3 (9), 503–509.

Wang, L.V., Hu, S., 2012. Photoacoustic tomography: in vivo imaging from organelles to organs. Science 335 (6075), 1458–1462.

Wang, L., Li, G., Xia, J., Wang, L.V., 2015. Ultrasonic-heating-encoded photoacoustic tomography with virtually augmented detection view. Optica 2 (4), 307–312.

Wang, L., Maslov, K., Wang, L.V., 2013. Single-cell label-free photoacoustic flowoxigraphy in vivo. Proc. Natl. Acad. Sci. 110 (15), 5759–5764.

Wang, L.V., Wu, H.I., 2012. Biomedical Optics: Principles and Imaging. John Wiley and Sons.

X. Yang, X., Skrabalak, S.E., Li, Z.Y., Xia, Y., Wang, L.V., 2007. Photoacoustic tomography of a rat cerebral cortex in vivo with au nanocages as an optical contrast agent. Nano Lett. 7 (12), 3798–3802.

Xi, L., Grobmyer, S.R., Zhou, G., Qian, W., Yang, L., Jiang, H., 2012. Molecular photoacoustic tomography of breast cancer using receptor targeted magnetic iron oxide nanoparticles as contrast agents. J. Biophotonics 7 (6), 401–409.

Xu, M., Wang, L.V., 2006. Photoacoustic imaging in biomedicine. Rev. Sci. Instrum. 77 (4), 041101.

Zhang, Q., et al., 2009. Gold nanoparticles as a contrast agent for in vivo tumor imaging with photoacoustic tomography. Nanotechnology 20 (39), 395102.